JOURNAL OF CATALYSIS 129, 473–485 (1991)

Microstructures of Pt–Sn and Rh–Sn Particles on SiO_2[1]

T. P. CHOJNACKI[2] AND L. D. SCHMIDT

Department of Chemical Engineering and Materials Science, University of Minnesota, Minneapolis, Minnesota 55455

Received September 19, 1990; revised January 21, 1991

The effect of adding Sn to Pt and Rh particles on SiO_2 is examined by transmission electron microscopy following heat treatments in H_2 and O_2 atmospheres. With both metals, after heating in H_2, no fcc metal is observed but rather a series of intermetallic compounds with multiple phases coexisting within most 20 to 200-Å particles. The surfaces of these particles are the Sn-rich MSn_4 phases. When Pt–Sn is oxidized, the only phases observed are Pt metal and SnO_2. Dark field imaging shows that the SnO_2 forms 10 to 30-Å crystals which surround the single-crystal Pt particles and are in contact with the SiO_2. When Rh–Sn is oxidized Rh, Rh_2O_3, and SnO_2 are detected, but SnO_2 forms before Rh_2O_3, and the presence of Sn retards the oxidation of Rh.

INTRODUCTION

Additives play an essential role in controlling the activity, selectivity, and stability of most noble metal catalysts (*1, 2*). While Sn itself has little catalytic activity, it is used as an additive in several catalytic processes. In naphtha reforming the addition of Sn to Pt greatly increases performance and lifetime (*3–6*). In recent studies, Rh–Sn/SiO_2 was found to be extremely active and selective toward the reduction of ethyl acetate to ethanol (*7*). Other studies found that Sn produced large changes in the activity of Rh/SiO_2 toward benzene hydrogenation, and propane hydrogenolysis (*8*). The presence of Sn in Pt/SiO_2 was found to increase the thermal stability of the catalyst (*9*) while others found that the surface of Pt–Sn catalysts was enriched with Sn which catalyzed the reversible adsorption of ethene (*10*).

Interpretation of the exact nature of these bimetallic catalysts is complicated by the fact that the Pt–Sn and the Rh–Sn systems both form five intermetallic compounds (see Table 1) and that Sn can exist in three oxidation states, Sn^0, Sn^2, and Sn^4. This has led to considerable debate about the chemical state of the Sn species in these catalysts. Dautzenburg *et al.* (*11*) proposed that these bimetallic catalysts consist of alloys with Sn in the zero valent state, while others using Mossbauer spectroscopy (*12*) showed evidence of Pt–Sn alloys, Sn^4, Sn^2 with Pt not alloyed with tin. Recent studies indicate that the valence state of Sn in noble metal catalysts is dependent upon the support (*13, 14*).

In the present work, we examine by transmission electron microscopy (TEM) the structures of the bimetallic catalysts Pt–Sn and Rh–Sn/SiO_2 and the structural changes which occur as a result of various thermal treatments. TEM is uniquely suited to determine the microstructure of particles on a 10-Å scale. However, the systems used here, while good models of real catalysts, are prepared from evaporated films of the materials on planar amorphous SiO_2 films. They should therefore differ from real catalysts in size of particles and support morphology, as well as other factors.

[1] This research partially sponsored by NSF under Grant No. CBT88822745.

[2] Present address: Cray Research, Chippewa Falls, WI.

0021-9517/91 $3.00

TABLE 1

Possible Compounds and Phases Pt–Sn and Rh–Sn

Metal	H_2 Treatment	O_2 Treatment
Pt	$PtSn^a$(hex)[a]	$SnO_2{}^a$(tetrag)[h]
	$PtSn_2$ (fcc)[b]	SnO_2 (ortho)[i]
	$PtSn_4{}^a$(ortho)[c]	Sn_2O_3 (triclinic)[j]
	Pt_2Sn_3 (hex)[d]	Sn_3O_4 (triclinic)[k]
	Pt_3Sn^a(fcc)[e]	$SnSiO_3$ ()
	α-Sn (fcc)[f]	
	β-Sn (tetrag)[g]	
Rh	RhSn (fcc)[c]	$SnO_2{}^a$
	$RhSn_2$ (tetrag)[c]	SnO_2
	$RhSn_4{}^a$()	Sn_2O_3
	Rh_2Sn^a()	Sn_3O_4
	$Rh_3Sn_2{}^a$()	$SnSiO_3$
	α-Sn	
	β-Sn	

Note. ASTM, "X-ray Powder Diffraction Data Files," and Ref. (*21*).

[a] Indicates phases observed here.

EXPERIMENTAL

Samples were 50 to 200-Å particles of the noble metal on ~200-Å planar films of amorphous SiO_2, as described previously (*15, 16*). SiO_2 films were first prepared by vacuum depositing Si onto a Formvar film on gold TEM grids. This sample was then heated in air at 600°C to remove the Formvar and oxidize the Si to a uniform layer of amorphous SiO_2. Noble metals were deposited by vacuum deposition of the pure metals to a thickness (~10 Å) which formed particles of suitable size and density when heated to 600°C in a H_2 atmosphere.

Sn was then deposited on one-half of the microscope grid by masking part of the grid during Sn deposition. In this manner, each grid had the bimetallic system on one half and the corresponding pure noble metal on the other half for comparison. Several samples of each system were prepared. Metal loading was controlled by monitoring the film thickness with a quartz crystal microbalance and converting these thicknesses into atomic ratio. Metal ratios in samples examined ranged from 0.5 to 2, although all results shown are for single samples of each with Sn/Pt = 0.7 and Sn/Rh = 1.0. At least five samples of each combination were examined, and all results reported were consistent between samples.

Metallic Sn melts at 232°C, but its vapor pressure is $<1 \times 10^{-9}$ Torr at 600°C. Therefore, we expect that, while Sn should be mobile under reducing conditions, losses by evaporation should be insignificant. Sn was not observed to migrate over macroscopic distances as noted from the absence of Sn on the half of the grid on which it was not deposited.

Samples were heated in a quartz tube furnace in flowing ultrahigh purity gases at atmospheric pressure and were analyzed in a JOEL 100CX TEM. Samples could be transferred repeatedly between the tube furnace and the microscope such that *the same particles* could be examined repeatedly after sequential treatments in different gas atmospheres (*15, 16*).

We used the technique of unsharp masking (*17*) to reduce contrast and observe weak features in TEM images and electron diffraction patterns. By making prints which are a superposition of the negative and an out of focus positive, one can observe features and diffraction lines which are a small fraction of major features. Note that the contrast in TEM is approximately proportional to total electron density. Since atomic numbers of Pt, Rh, Sn, Si, and O are 78, 45, 50, 14, and 8, respectively, one expects Pt to have more contrast than Sn, Rh to be comparable to Sn, and Si and O to be nearly invisible for comparable thicknesses. For crystalline phases, diffraction contrast is significant and prevents thickness determination from contrast alone; however, thickness contrast is sufficiently different for these compounds that they are easily identified from the micrographs and from dark-field images.

RESULTS

Platinum–Tin

Figures 1–3 show a sequence of micrographs of a typical sample containing Sn/Pt = 0.7. Arrows in each figure mark *the same*

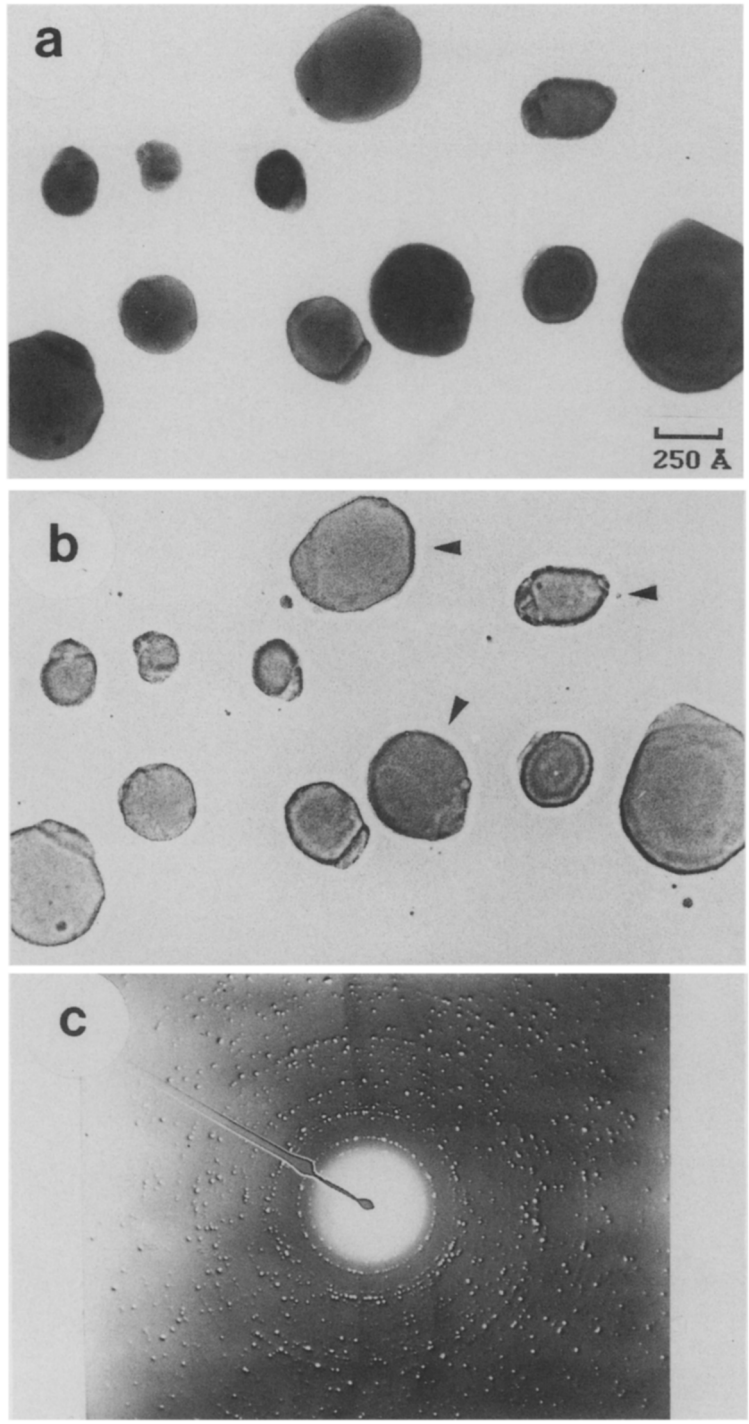

FIG. 1. (a) Typical bright-field TEM image of Pt–Sn particles on thin planar amorphous SiO_2 with Sn/Pt = 0.7 formed from thin films of the metals after H_2 treatment at 650°C for 18 hr. The average particle size is ~100 Å. Particles are nearly opaque, indicating contrast of the particles much higher than that of the SiO_2 film. This is the same region shown in Figs. 2 and 3 after treatments indicated. (b) Same image as (a) printed using unsharp masking which reveals internal grain boundaries and multiple crystals in most particles. (c) The diffraction pattern of (a) and (b), also printed using unsharp masking to reveal low-contrast features. This pattern contains many spots and rings, indicating the presence of many crystalline phases. Indexing this pattern shows the presence of the intermetallics PtSn, $PtSn_4$, and Pt_3Sn but no fcc Pt.

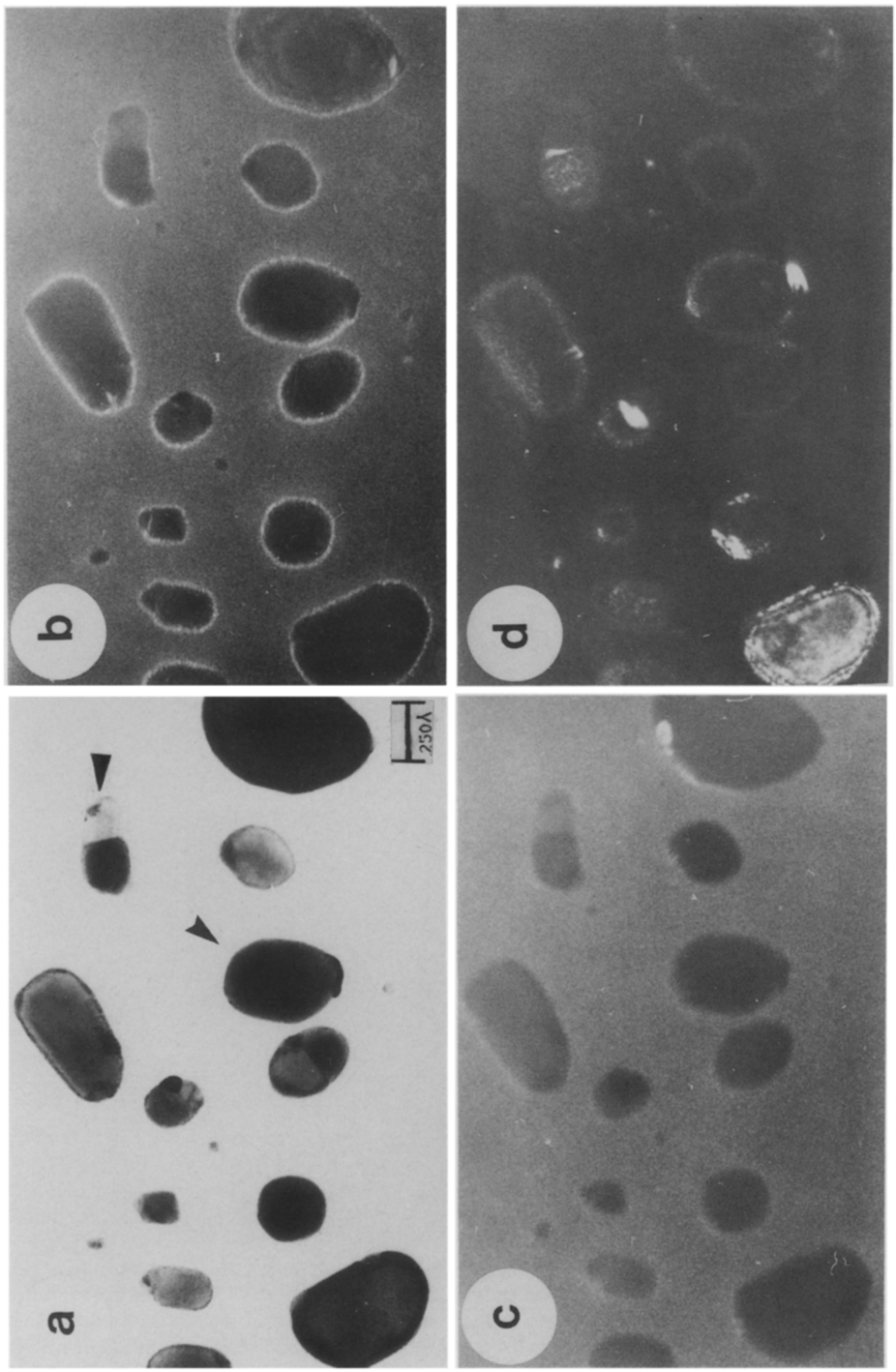
a
250Å
b
c
d

particles. Figure 1 shows a sample after H_2 treatment at 650°C for 18 hr. This micrograph is in fact after the treatments of Figs. 2 and 3. Figure 1a shows a normal micrograph, while Fig. 1b shows the same image developed using unsharp masking (*17*) which reduces contrast and reveals grain boundaries within particles. This micrograph illustrates the typical structures of Pt–Sn particles after treatment in H_2. Most particles show one or more sharp grain boundaries separating distinct regions or phases. The accompanying diffraction pattern in Fig. 1c, also developed using unsharp masking (*17*), shows many rings and spots which are associated with diffraction rings. These are all assignable to the intermetallic phases of PtSn, Pt_3Sn, and $PtSn_4$. The diffraction pattern reveals *no rings of fcc Pt metal*, even with increased contrast by unsharp masking; we estimate that the limit of detectability would correspond to ~5% fcc Pt.

Figure 2 shows the same sample as that shown in Fig. 1 after the initial treatment in H_2 at 650°C for 18 hr. These particles exhibit several phases in each particle like those in Fig. 1, and the diffraction pattern indicates the presence of at least three intermetallic phases: PtSn, Pt_3Sn, and $PtSn_4$.

Dark field imaging of the particles in Fig. 2a using the (112) reflections of $PtSn_4$ (Fig. 2b) shows that this phase forms several small crystallites. In addition, the edges of all particles "light up," indicating that the entire surface layer of all particles is in fact $PtSn_4$. The dark-field image using the (101) ring of PtSn is shown in Fig. 2c. Only two crystallites satisfy the diffraction condition in this micrograph, but other dark-field images indicate that the major phase in most particles is the intermetallic PtSn. Figure 2d is a dark field image of these same particles using the (220) ring of $PtSn_4$ and the (111) reflections of Pt_3Sn and the (102) reflections of the intermetallic PtSn. The majority of each particle appears to be composed of PtSn with the regions of high intensity a result of the characteristically intense first reflection of the fcc Pt_3Sn, and the weak intensity coming from the small crystallites of $PtSn_4$.

The micrograph in Fig. 2d, which includes the (102) reflection of the intermetallic PtSn, exhibits one particle which satisfies the weak beam condition for this reflection and therefore reveals thickness fringes in this particle. This shows that this particle is three dimensional and its morphology is roughly hemispherical. This example and others not shown confirm the generally spherical shapes of these multiphased particles.

When the sample of Fig. 2 is heated in O_2 at 550°C for 1 hr following the initial H_2 treatment, all particles undergo a radical change in shape and structure. Figure 3a (same particles as Fig. 2 indicated by arrows) shows that all particles have expanded in size and are composed of a high-contrast core with an outer layer of low-contrast material surrounding the core. The diffraction pattern (Fig. 3b) reveals that all intermetallic species have disappeared and

FIG. 2. Micrographs of Pt–Sn/SiO_2 for a sample with Sn/Pt = 0.7 after treatment in H_2 at 650°C for 18 hr. (a) The bright field image with unsharp masking shows that most particles have several phases. (b) Dark field image of (a) using the (112) reflection of $PtSn_4$. This shows a region at the edge of each particle which "lights up," indicating that the surface layer of each particle contains microcrystalline region of $PtSn_4$. (c) Dark field image of (a) using the (101) reflection of PtSn showing two crystallites that satisfy the diffraction condition. In fact, most particles contain regions of this phase. (d) Dark field image of (a) using the $PtSn_4$ (220), the Pt_3Sn (111), and the PtSn (102) reflections. The fine structure of $PtSn_4$ is also present at the edges and on top of the particles, confirming that this species covers the entire surface of the particles. The intense regions of illumination are regions of Pt_3Sn, resulting from the characteristically strong (111) reflection of fcc materials. The large particle in the lower left corner satisfies a weak beam condition for the PtSn (102) reflection. The thickness fringes seen in this particle show the contour of the particle which is generally spherical in shape.

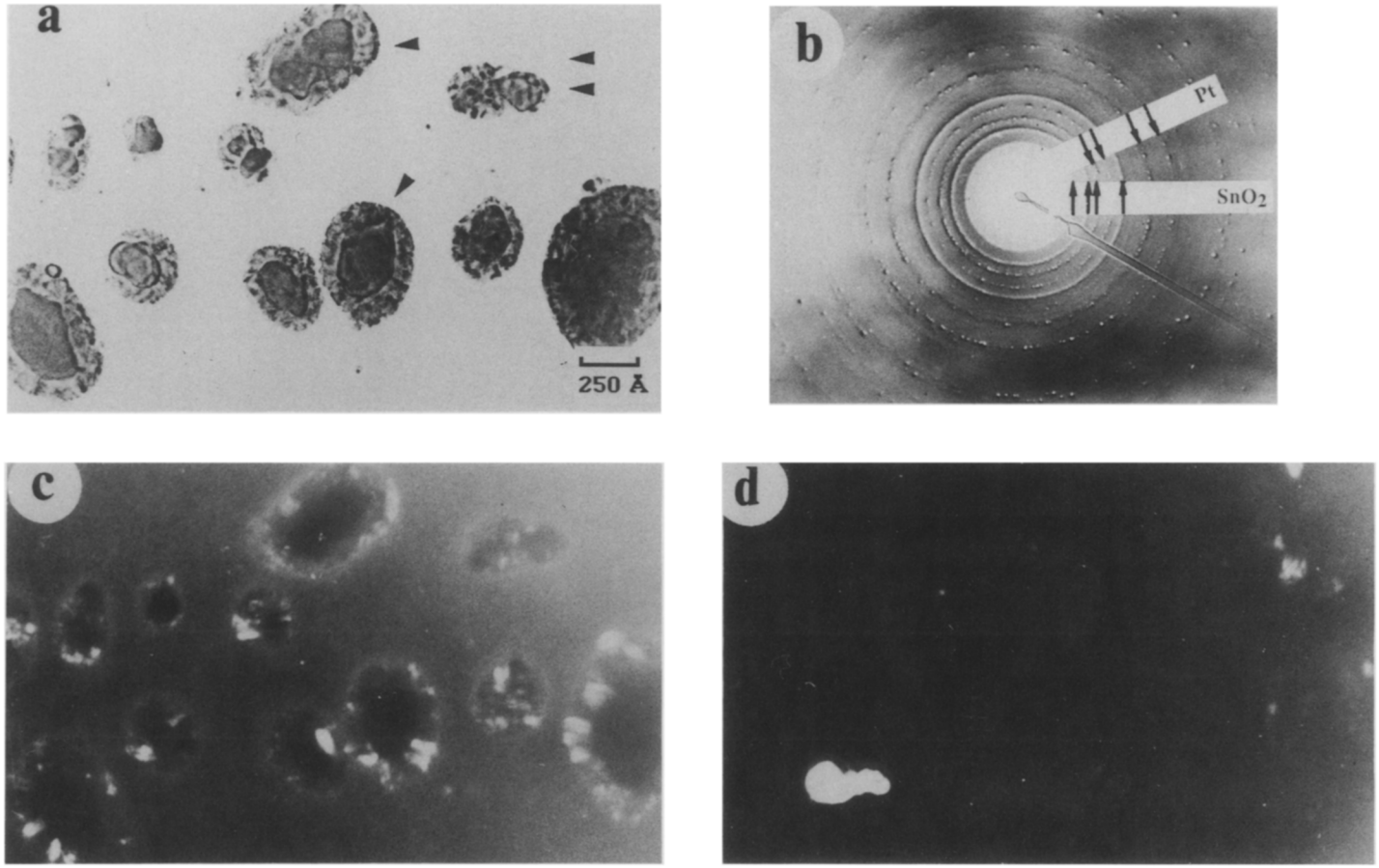

FIG. 3. Micrographs of Pt–Sn/SiO_2 showing the same particles in Fig. 2 after treatment in O_2 at 550°C for 1 hr. (a) Bright field image shows the particles to be composed of a high-contrast core covered by lower-contrast material. (b) The diffraction pattern of (a) indicates the presence of Pt metal and SnO_2 as the only crystalline phases. Some of the rings of these phases are labeled. (c) A dark field image of (a) using the (110) reflection of SnO_2 confirms that the outer material is microcrystalline SnO_2. (d) Dark field imaging using the (200) ring of Pt shows the core material to be Pt metal, although only a single particle satisfies the diffraction condition in this micrograph.

are replaced by SnO_2 (cassiterite) and all Pt is now present as fcc Pt metal. Dark field imaging using the (110) ring of SnO_2 (Fig. 3c) shows the low-contrast material to be crystalline SnO_2 and that some of the oxide covers the top of the Pt cores as well as around them. However, most SnO_2 appears to surround the Pt particles and to be in contact with the SiO_2. No measurable deviation from the lattice constant of pure Pt particles was found. The use of the Pt(200) ring in dark field imaging confirms that the cores of the particles consist only of Pt (Fig. 3d).

Further treatment of the oxidized samples of Fig. 3 in H_2 at 650°C caused the particles to return to their original multiphase structure assumed after the initial H_2 treatment, and this micrograph is shown in Fig. 1. This structure is also one in which the bulk of each particle is composed of the intermetallic PtSn with inclusions of $PtSn_4$ and Pt_3Sn and covered by a thin shell of $PtSn_4$. The diffraction pattern also reverted to the pre-oxidation pattern of PtSn, Pt_3Sn, and $PtSn_4$. Dark field imaging (not shown) confirms this structure and argues that this is the equilibrium structure of the reduced particles because it forms from both the initial films and the oxidized particles. Note, however, that particles are in the same general location and have the same size as in Fig. 2, although all particles have changed shape, and grain boundaries are in different positions after the phase transformations produced by oxidation, reduction, and reoxidation.

Rhodium–Tin

Figure 4 shows a sequence of micrographs of Rh–Sn on SiO_2 for Sn/Rh = 1.0. Heating of Rh–Sn films for several hours in hydrogen at 650°C produced generally round (hemispherical) particles which are composed of several intermetallic compounds of Rh and Sn, similar to those formed from Pt–Sn films under conditions identical to those shown in Fig. 4a. One observes an outer layer ~20 Å wide of lower contrast material that encloses an inner part of each ~200-Å particle. The cores of particles have regions of different contrast, indicating multiple phases and/or crystals. The accompanying diffraction pattern of this sample (Fig. 4c) has even more rings than that of Pt–Sn, indicating the presence of many Rh–Sn intermetallic compounds. However, no rings could be assigned to Rh–Sn although the pattern did confirm the presence of Rh_3Sn_2 and $RhSn_2$. The number and close proximity of rings in the diffraction pattern precluded any useful application of dark field imaging to identify the exact composition of the inclusions or of the outer material, although by analogy with Pt we expect the outer region to be Sn-rich phases.

Exposure of the Rn–Sn particles of Fig. 4a to O_2 at 550°C for 1 hr causes the particles to expand parallel to the silica surface as a result of the formation of oxides which have lower contrast than the metal particles as shown in Fig. 4b. Comparison of Figs. 4a and 4b shows that some regions of the particles appear to have a higher resistance to oxidation that others as noted by the arrows. It is also evident from fig. 4b that the outermost layer of these particles is composed of a low-contrast oxide. The diffraction pattern of the oxidized Rh–Sn sample (Fig. 4d) shows that this treatment results in the formation of both SnO_2 and Rh_2O_3, but the presence of the rings of fcc Rh metal shows that oxidation is not complete after treatment in O_2 at 550°. The Rh metal is present mostly as small, high-contrast particles interspersed throughout the oxide. Prolonged heating in O_2 produces complete oxidation of the Rh as indicated by the absence of rings assignable to Rh in the diffraction pattern. Dark field imaging using the (110) ring of SnO_2 confirms that SnO_2 was the dominant species in the outer layer of the particles (Fig. 4f).

As with the Pt–Sn particles, H_2 reduction of the oxide at 650°C for 2 hr results in transformation of oxide particles back into multiphase particles which were formed on the initial H_2 treatment of the Rh–Sn films as shown in Fig. 4e. It should be noted that this transformation occurs at the expense of the

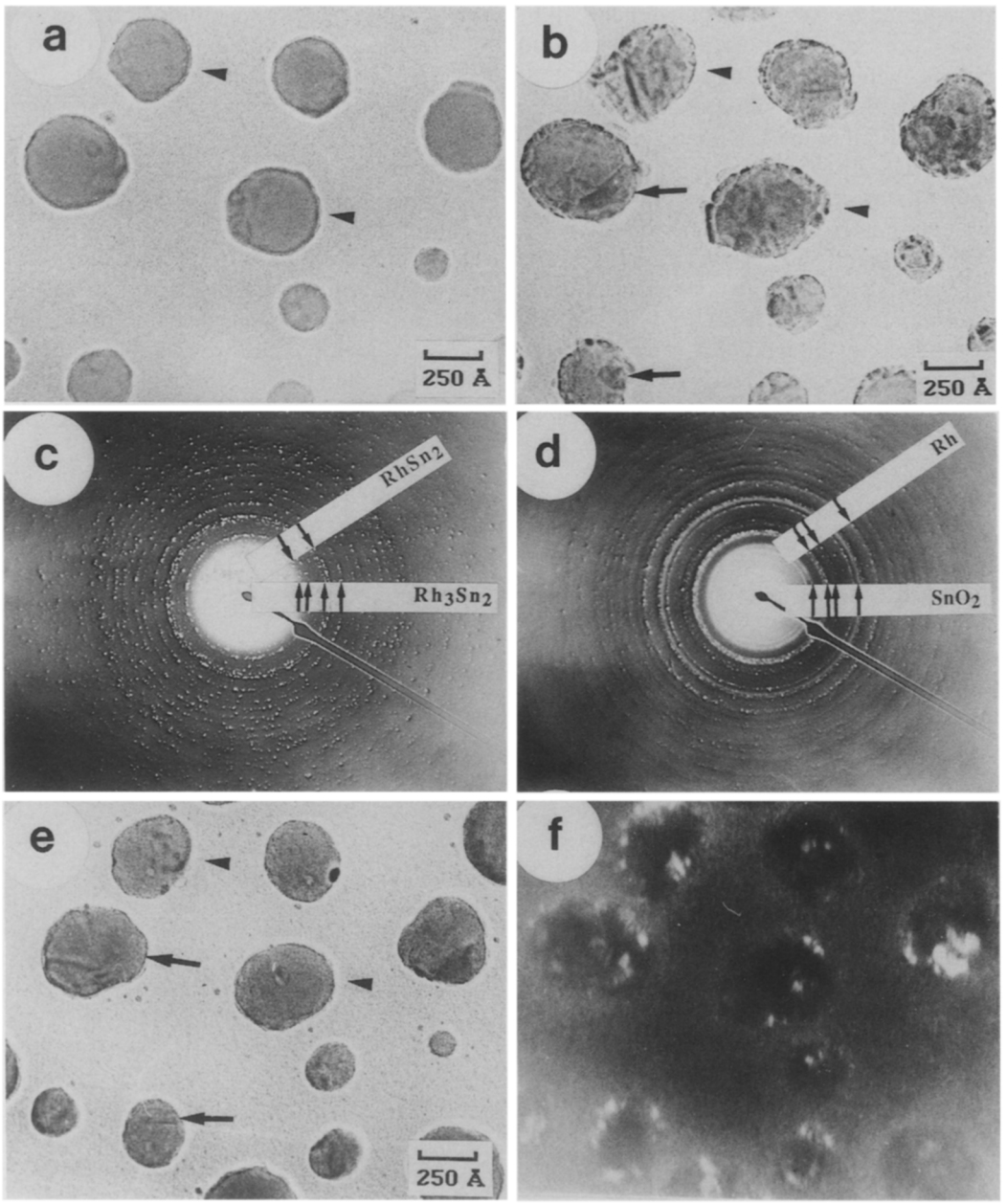

FIG. 4. (a) A micrograph of Rh–Sn/SiO_2 with Sn/Rh = 1.0 formed after heating Rh and Sn films in H_2 at 650°C for 2 hr. Microstructures are essentially identical to Pt–Sn, Figs. 1 and 2. (b) Micrograph of particles shown in Fig. 4 of Rh–Sn/SiO_2 after heating in O_2 at 550°C for 1 hr. All particles have internal microstructures and all are surrounded by rings of lower-contrast microcrystalline material. (c) The diffraction pattern of (a) which shows many intermetallic phases. Major ring positions of $RhSn_2$ and Rh_3Sn_2 are indicated. (d) Diffraction pattern of (b) which shows rings corresponding to Rh metal, Rh_2O_3, and SnO_2. (e) Micrograph of particles shown in (b) after reduction of the oxidized sample in H_2. Shapes are generally similar to those in (a), although shapes and locations of grain boundaries are different. (f) Dark field image of the sample shown in (b) using the (110) diffraction line of SnO_2. This shows that the low-contrast ring surrounding each particle is SnO_2, just as for Pt–Sn for similar treatment. The cores of particles contain Rh, Rh_2O_3,and SnO_2.

small, dispersed oxide particles which apparently migrate to the larger particles since there are no small reduced particles at the locations where the small oxide particles were located before the H_2 treatment. The internal structure of the resultant particles is essentially the same as before the O_2 treatment, although the exact shape of the particles is changed, as expected, because all have gone through two phase transitions.

After exposure to O_2 at ~600°C for 18 hr, one observes the formation of small oxide particles ≤20 Å in diameter near the periphery of the parent oxide particles (Fig. 5a). This is the same sample as in Fig. 4, but a different region is shown. In addition, many smaller (~10 Å diameter), low-contrast particles form which are uniformly dispersed over the SiO_2. After continued heating in O_2, the size and number of these small particles increases, and they disperse onto the field of the support (Fig. 5b). This dispersion, which increases with heating time at these temperatures, was not found in samples of pure Rh/SiO_2 when treated in O_2. It was not observed in the O_2-treated Pt–Sn samples, although this may have been because of inadequate heating time and temperature. Evidently, SnO_2 begins to move away from the large particles with continued heating, although high temperatures and long times appear necessary for complete separation of metal and Sn.

DISCUSSION

In Fig. 6 are sketched the idealized top and side views of the microstructures we infer from these experiments for Pt–Sn. Rh–Sn is essentially identical after heating in H_2, but Rh_2O_3 forms after heating in O_2. We of course only observe structures parallel to the substrate and must infer perpendicular dimensions from contrast and in some cases from weak beam interference fringes (Fig. 2). Microstructures and phases are quite different after heating in H_2 and O_2 as expected because of the ease of oxidation and reduction of Sn and the different chemical properties of Sn and SnO_2.

However, the noble metal–Sn systems appear to be simpler than many other alloy systems in that the Sn does not seem to form any compounds or interact strongly with the SiO_2. Therefore the SiO_2 can be regarded simply as a support for the multicomponent particles with interactions coming primarily from different interfacial energies between phases. This is in contrast to additives such as Ce (*18, 19*) which form amorphous phases and interact strongly with the SiO_2 under reducing conditions to form a continuous film.

Also, we see little evidence of noncrystalline phases, either as three-dimensional compounds or as films. All structures appear to be identifiable as known crystalline phases, although very thin or small regions (<10 Å) may be unnoticed if their contrast is small.

Structures after Hydrogen Treatment

Under reducing conditions the only phases observed are intermetallics, which constitute perhaps all phases in published phase diagrams for Pt–Sn and Rh–Sn, although the diffraction patterns are sufficiently complex that we did not detect several phases that have been reported. For Pt and Rh we see no diffraction patterns of the metals for Sn/metal ratios as low as 0.5. We did not examine lower Sn loadings which must obviously produce the metal phase. Pt and Rh microstructures after H_2 treatment appear to be essentially identical, as expected because the intermetallic phase diagrams are very similar, their interactions with SiO_2 are similar, and the temperatures where particles can change shape are only slightly higher for Rh than Pt[15].

We see multiple phases in all 50 to 300-Å diameter particles (Fig. 6). If the Sn/metal ratio were constant in all particles, one would expect two phases to form by the Lever Rule because the mutual solubility of one phase in another appears to be small. The observation of many phases is consistent with the variability of composition between particles determined by statistical

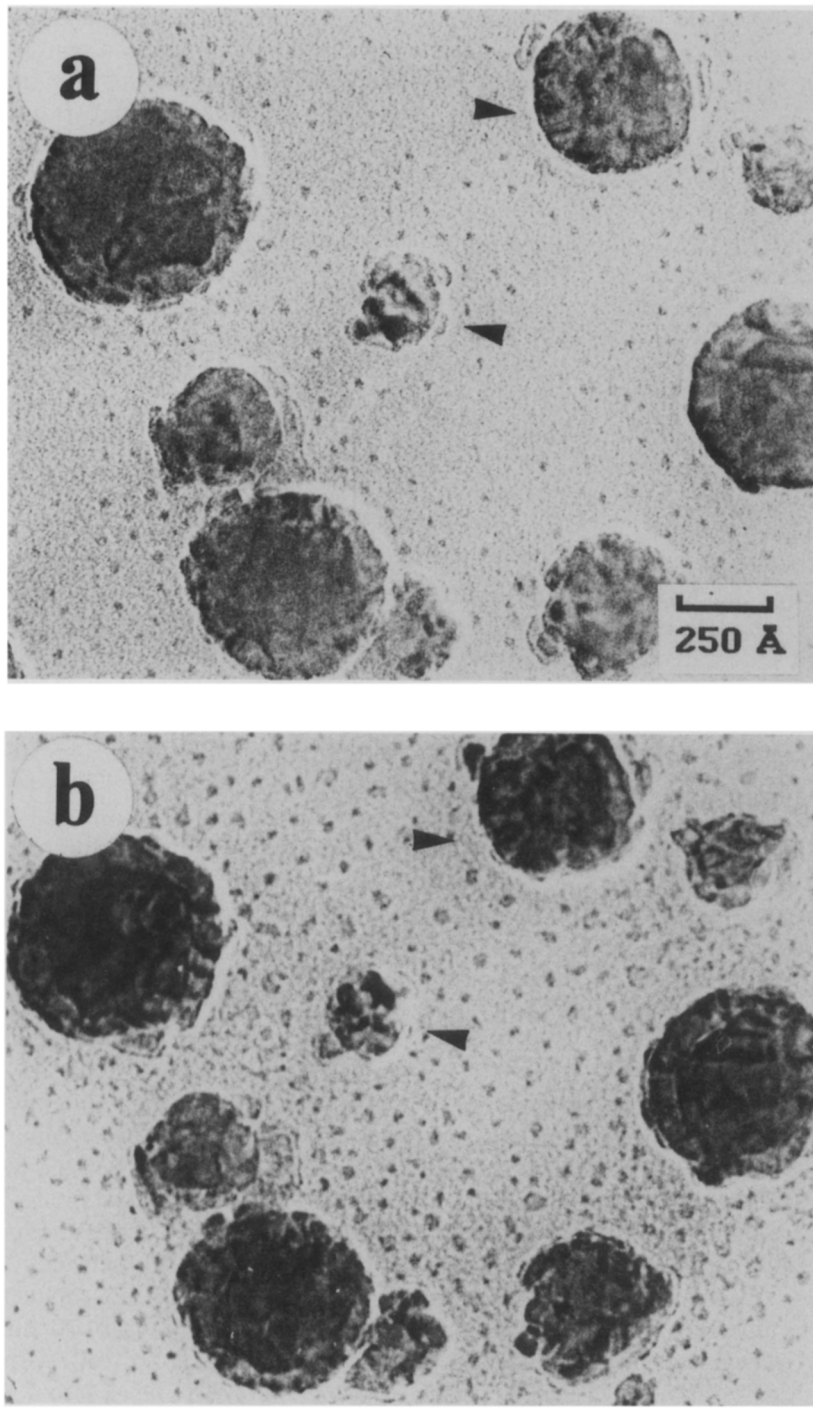

FIG. 5. (a) Micrographs of Rh–Sn/SiO_2 for Sn/Rh = 1.0 after treatment initial treatment in H_2 to form intermetallic particles followed by heating in O_2 at 550°C for 18 hr. This is a different region than that shown in Fig. 4. Structures are essentially identical to those shown in Fig. 4 although some small particles are now seen dispersed over the substrate. (b) Micrograph of the same particles after further heating. Microstructures of large particles are changed only slightly, but the regions between particles now contain small (10–20 Å diameter) particles.

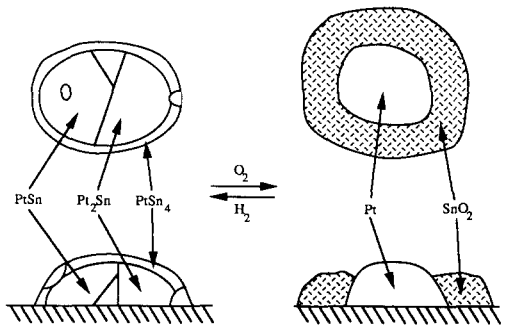

FIG. 6. Illustrations of the idealized morphologies of the Pt–Sn particles on silica. (a) The Pt–Sn particles form multiple phases containing PtSn, Pt_3Sn, and $PtSn_4$ with an outer layer of microcrystalline $PtSn_4$ when treated in H_2. (b) When treated in O_2, SnO_2 forms on the outside of the particles leaving a core of Pt metal at the center.

fluctuations and in the local variations on SiO_2 during growth. In addition, we observe three phases in many particles. This requires that, even within a single particle, metal and Sn atoms do not form a uniform distribution under the annealing conditions of these experiments, several hours at 600°C.

All particles are covered by a thin layer of microcrystalline MSn_4. This is consistent with the surface free energies of the phases which should be lower for the high Sn phases. Of course, one expects the surface layer in any alloy or compound to be enriched with whatever components will minimize the free energy, and in this situation this appears to be a distinct phase. Surfaces should also be expected to be enriched in high Sn phases whenever they are formed from oxidized catalysts because SnO_2 forms preferentially over the metal cores of particles. After chemical reduction from Sn^4 to Sn^0, which probably occurs very quickly near the surfaces of particles, migration of Sn through other phases into the interior of particles requires bulk diffusion and is driven by the small free energy differences between the intermetallic phases.

Structures after Oxidation

Microstructures of Pt–Sn and Rh–Sn particles are of course different under oxidizing conditions because Rh oxidizes while Pt does not. However, with both metals SnO_2 grows as a microcrystalline ring (~20-Å crystals) around the original intermetallic particle.

For Pt the microstructure in O_2 is fairly simple: Pt particles surrounded by SnO_2 crystals are shown in Fig. 6. The Pt particles generally appear to be single crystals with few grain boundaries or twins. This suggests that there is little Sn^0 present as Pt crystals grow from the intermetallics because the presence of any solutes generally causes growth mistakes. As examples, the presence of Na, Zn, or Ce (*18, 19*) produces Pt particles which have many internal defects when grown under these conditions. Evidently the Sn quickly forms SnO_2 which leaves the Pt to crystallize as defect-free particles.

For Pt–Sn the SnO_2 appears to form mainly as a ring around the metal particle with very little SnO_2 on top of the metal particles or within them. One expects the oxide to form on the surface of the metal because it has a lower surface free energy and Sn is more mobile than Pt and therefore can easily migrate to the surface to react with O_2. The formation of a ring of SnO_2 indicates that $\gamma_{SnO_2-SiO_2}$ is less than γ_{SnO_2-Pt}.

For Rh–Sn the initial oxidized structures appear to be similar to those of Pt with a ring of SnO_2 surrounding Rh metal. However, continued heating and higher temperatures causes oxidation of Rh to Rh_2O_3. These oxide phases have very low surface-free energies compared to the metals and both phases "wet" or spread out onto the SiO_2, although the driving force for this migration is small and the process is slow even at 600°C. The small particles on the SiO_2 for Rh–Sn after long heating (Fig. 5) indicate considerable mobility of SnO_2 on the SiO_2.

The presence of Sn retards the oxidation of Rh in that we observe Rh metal after heating to 600°C in O_2 in the presence of Sn, while pure Rh particles would be immediately oxidized under these conditons. Evidently SnO_2 forms a protective coat over the Rh which retards its oxidation.

Comparison with Real Catalysts

We emphasize that the systems used here, 20 to 200-Å particles on planar amorphous SiO_2, are quite different from the corresponding Pt–Sn porous supported catalysts (which are also more often supported on Al_2O_3). One should expect Sn and Rh to be more easily reduced on SiO_2 than on Al_2O_3 because of the stronger interactions of all oxides with Al_2O_3 (*1, 2, 5, 20*). Our particle sizes are generally much larger than those used as catalysts, and our supports are planar and therefore have no channels or pores in which to stabilize particular structures. The SiO_2 in these experiments was grown from Si by heating in O_2 and therefore initially contains no surface OH groups which can interact differently with the particles.

However, these results represent a prototype of the microstructures expected in the porous catalyst systems. The structures seen here represent the microstructures for larger particles on highly inactive SiO_2. For real catalysts consisting predominantly of clusters containing only a few atoms one should expect different and more complex interactions. The surface of our larger particles probably also have similar geometries and interactions to those of smaller particles. Thus, one difference between structures we observe and those reported in the literature for real catalysts should be due to the larger particle sizes we use. However, techniques such as XRD, EXAFS, and Mossbauer spectroscopy have different sensitivities to differnt aspects of structures. For example, XRD detects diffraction patterns only for particle sizes >100 Å, while in TEM diffraction is observed for crystallite sizes >10 Å. TEM is capable of "seeing" all structures whose contrast is sufficiently large. The major limitation of TEM is its inability to observe structures smaller than 10 Å, the regime in which EXAFS and Mossbauer spectroscopy sample properties (and the scale which determines reaction site properties). However, both techniques detect mass-weighted averages so the presence of large particles can still obscure properties of smaller ones.

SUMMARY

These results clearly show that 20 to 500-Å binary alloy particles of Pt–Sn and Rh–Sn/SiO_2 when heated in H_2 are composed of several intermetallic compounds with a surface layer containing the most Sn-rich intermetallic phase. Furthermore, the phases present differ from those which might be expected from the Lever Rule as a consequence of surface enrichment. Catalysts with Sn additives usually are operated in strongly reducing conditions, so these results should be most directly applicable to this situation. Treatment in oxygen results in a dramatic change in the morphology as well as the composition of these particles in that SnO_2 forms on the surface of the particles because Sn is the more easily oxidized metal in both systems. Calcination of catalysts should tend to produce these microstructures.

REFERENCES

1. Ponec, V., *in* "Advances in Catalysis" (D. D. Eley, H. Pines, and P. B. Weisz, Eds.), Vol. 32 p. 1. Academic Press, San Diego, 1983.
2. Sinfelt, J. H., "Bimetallic Catalysts: Discoveries, Concepts, and Applications," Wiley, New York, 1983; *in*"Proceedings, 46th International Annual Meeting Electron Microscopy Society of America," p. 718, 1988.
3. Davis, B. H., *J. Catal.* **46,** 348 (1977).
4. Karpinski, Z., and Clarke, J. K. A., *J. Chem. Soc., Faraday Trans. 2* **71,** 893 (1975).
5. Szabo, G. L., *in* "Metal-Support and Metal-Additive Effects in Catalysis" (B. Imelik, *et al.*, Eds.). Elsevier, Amsterdam/New York, 1982.
6. Burch, R., and Garla, L. C., *J. Catal.* **71,** 360 (1981).
7. Candy, J. P., Ferretti, O. A., Mabilon, G., Bournonville, J. P., El Mansour, A., Basset, J. M., and Martino, G., *J. Catal.* **112,** 210 (1988).
8. Ermakov, Y. I., Kuznetsov, B. N., and Chelganov, E. M., *React. Kinet. Catal. Lett.* 14, 37 (1980).
9. Shepelin, A. P., Chernyshev, A. P., Kovalchuk, V. I., Zhdan, P. A., Yurchenko, E. N., Kuznetsov, B. N., and Ermakov, Y. I., *Kinet. Katal.* **22,** 716 (1981).
10. Verbeek, H., and Sachtler, W. M. H., *J. Catal.* **42,** 257 (1976).

11. Dautzenburg, F.M., Helle, J. N., Biloen, P., and Sachtler, W. M. H., *J. Catal.* **63,** 119 (1980).
12. Bacaud, R., Bussiere, P., and Figueras, F., *J. Catal.* **69,** 399 (1981).
13. Metizner, G., Via, G. H., Lytle, F. W., Fung, S. C., and Sinfelt, J. H., *J. Phys. Chem.* **92,** 2925 (1988).
14. Muller, A. C., Englehard, P. A., and J. E. Weisang, *J. Catal.* **56,** 65 (1979).
15. Chojnacki, T. P., and Schmidt, L. D., *J. Catal.* **115,** 473 (1989).
16. Lee, C. P., and Schmidt, L. D., *J. Electrochem. Soc.* **136,** 2471 (1989).
17. Hamilton, J. F., *J. Appl. Phys.* **39,** 5333 (1968).
18. Chojnacki, T. P., Krause, K., and Schmidt, L. D., *J. Catal.,* in press.
19. Chojnacki, T. J., Ph.D. thesis, University of Minnesota, 1989.
20. Burkhardt, J., and Schmidt, L. D., *J. Catal.* **116,** 240 (1989).
21. Massalski, T. B. Ed., "Binary Alloy Phase Diagrams," ASTM, 1986.